eLIFE
elifesciences.org

Figures and figure supplements

Mechanisms of organelle biogenesis govern stochastic fluctuations in organelle abundance

Shankar Mukherji, Erin K O'Shea

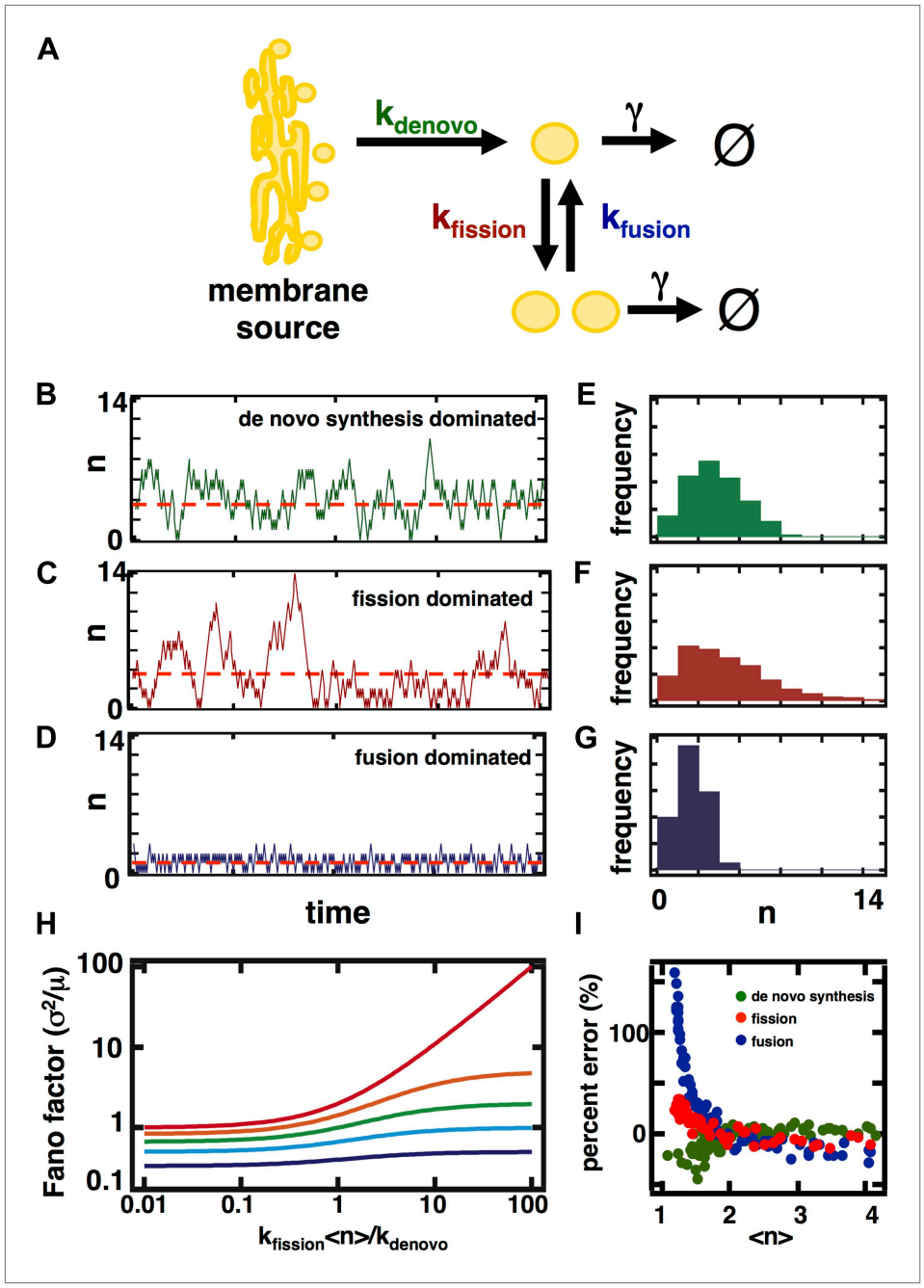

Figure 1. A stochastic model of organelle abundance dynamics. (**A**) Organelle abundances are governed by four distinct biophysical processes: (i) de novo synthesis ($k_{de\ novo}$, with units per time); (ii) fission ($k_{fission}$, with units per organelle per time); (iii) fusion (k_{fusion}, with units per organelle squared per time); and (iv) decay (γ, with units per organelle per time). (**B**) Sample trajectory generated by a Gillespie simulation of the model depicted in (**A**) in which the parameters are chosen to allow de novo synthesis to dominate over fission, fusion, and decay. (**C**) Sample trajectory as in (**B**), but with parameters chosen to allow fission to dominate over de novo synthesis, fusion, and decay. (**D**) Sample trajectory as in (**B**), but with parameters chosen to allow fusion to dominated over de novo synthesis, fission, and decay. (**E**) Histogram of the number of organelles generated by Gillespie simulations with parameters chosen as in (**B**). (**F**) Histogram of number of organelles generated by Gillespie simulations with parameters chosen as in (**C**). (**G**) Histogram of number of organelles generated by Gillespie simulations with parameters chosen as in (**D**). (**H**) Analytical approximation of the variance of the organelle abundance distribution divided by the mean of the distribution, or Fano factor, as a function of the ratio of the fission to de novo synthesis rate for various values of the fusion rate; from top to bottom the curves are calculated in order of

Figure 1. Continued on next page

Figure 1. Continued

increasing fusion rates: 0 (red), 0.25 (orange), 1 (green), 10 (cyan), 100 (blue). The value of **γ** is selected such that the mean organelle abundance is held constant for every point along these curves. (**I**) Percent error in the Fano factor prediction from the analytical approximation compared to Fano factor calculated from Gillespie simulations of the reaction scheme. The percent error is computed as the de novo synthesis (green dots), fission (red dots), and fusion (blue dots) rate constants are varied to tune the mean organelle abundance from $\langle n \rangle \approx 1$ to $\langle n \rangle \approx 4$, with the percent error between the prediction and simulation reaching close to 0% at $\langle n \rangle \approx 2$.

DOI: 10.7554/eLife.02678.003

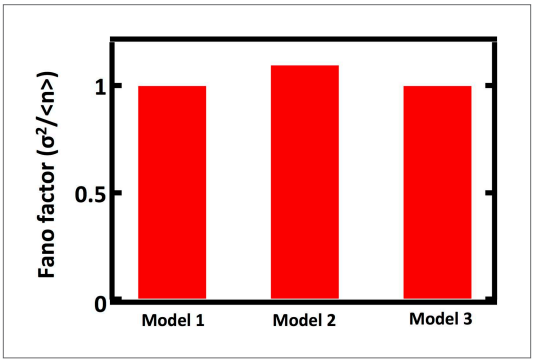

Figure 1—figure supplement 1. Comparison of Fano factors calculated from simulations of model with first order decay process (Model 1) with two alternative models substituting first order decay with partitioning at regular intervals.

DOI: 10.7554/eLife.02678.004

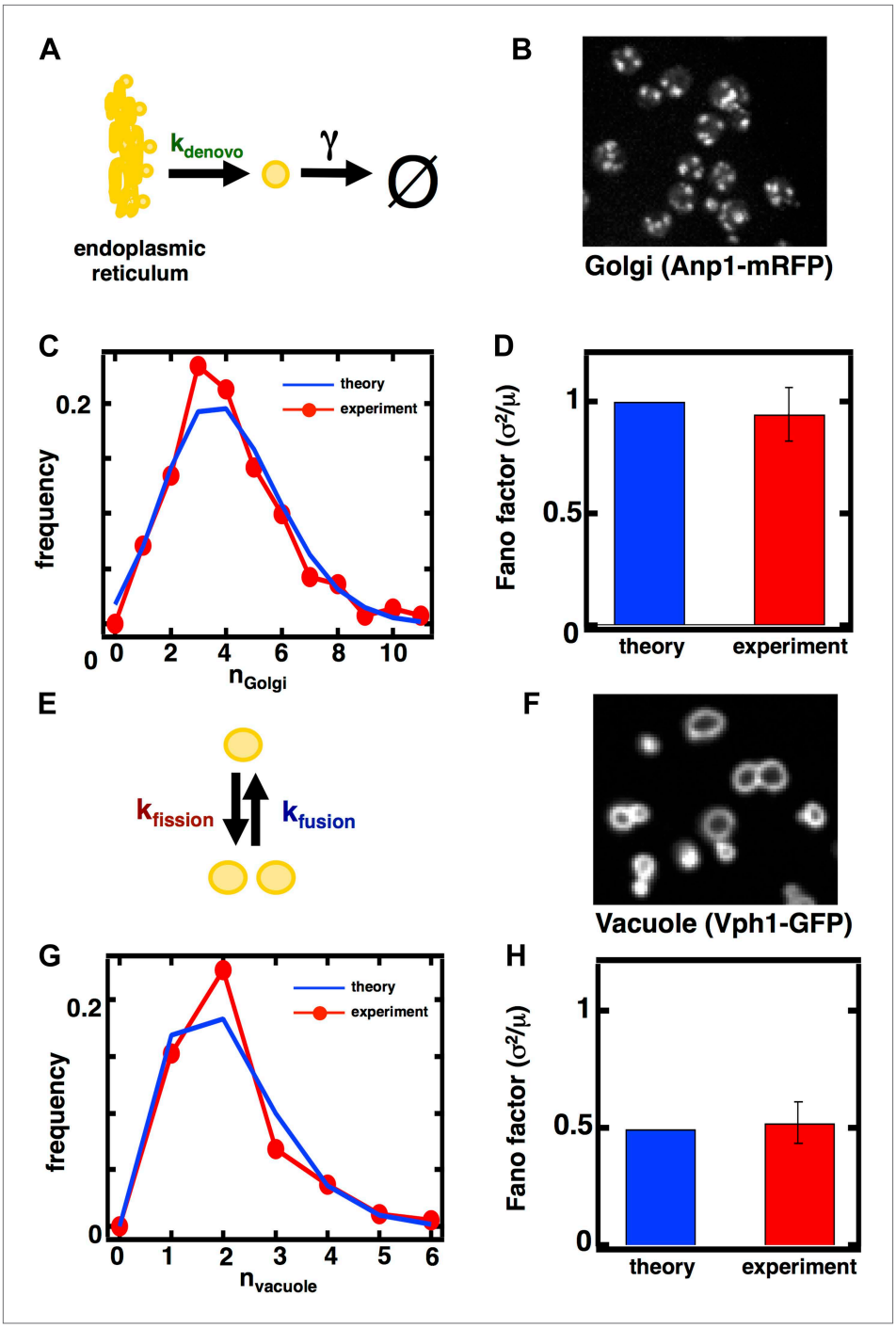

Figure 2. Predicting the stochastic fluctuations in Golgi apparatus and vacuole abundances. (**A**) Schematic depicting the biophysical processes that govern Golgi apparatus abundances. (**B**) Spinning disc confocal microscopy images of the Golgi apparatus as visualized by the fusion protein Anp1-mRFP. (**C**) Histograms depicting the theoretically predicted Golgi apparatus abundance distribution (blue trace) and experimentally measured single haploid cell Golgi apparatus abundance distribution (red trace). N = 141 cells were analyzed. (**D**) Bar graph depicting theoretical prediction (blue bar) and experimental measurement (red bar) of the Golgi apparatus abundance distribution Fano factor. (**E**) Schematic depicting the biophysical processes that govern vacuole abundances. Error bars are ±1 standard error of the mean, estimated by bootstrapping. (**F**) Spinning disc confocal microscopy images of the vacuole as visualized by the fusion protein Vph1 fused to green fluorescent protein (Vph1-GFP). (**G**) Histograms depicting the theoretically predicted vacuole abundance distribution (blue trace) and

Figure 2. Continued on next page

Figure 2. Continued

experimentally measured single haploid cell vacuole abundance distribution (red trace). N = 95 cells were analyzed. (**H**) Bar graph depicting theoretical prediction (blue bar) and experimental measurement (red bar) of the vacuole abundance distribution Fano factor. Error bars are ±1 standard error of the mean, estimated by bootstrapping.

DOI: 10.7554/eLife.02678.005

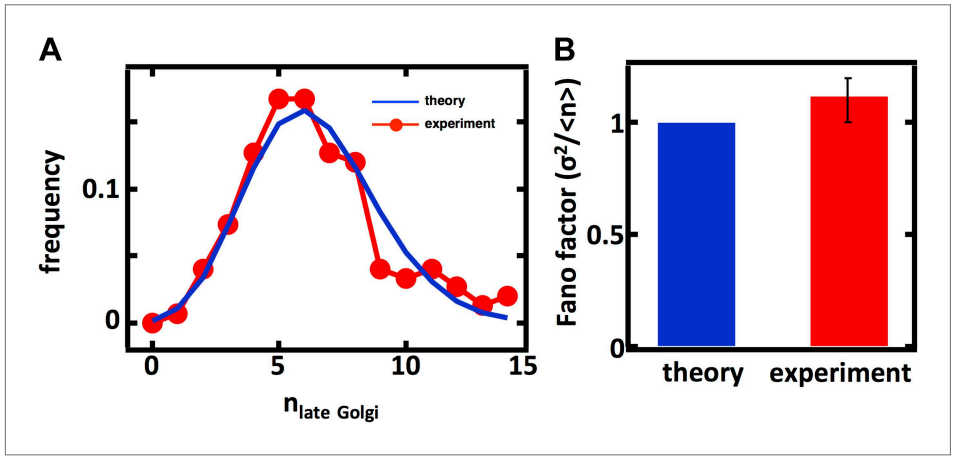

Figure 2—figure supplement 1. Predicting the stochastic fluctuations in late Golgi abundances.

DOI: 10.7554/eLife.02678.006

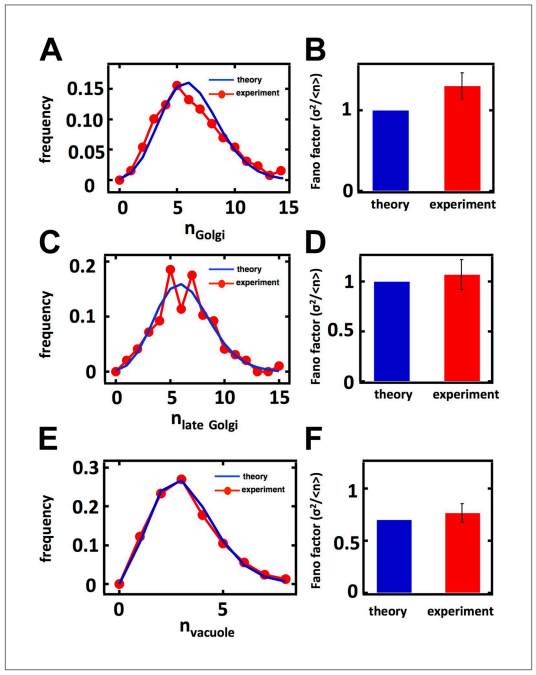

Figure 2—figure supplement 2. Predicting stochastic fluctuations in Golgi, late Golgi and vacuole abundance distributions in budding yeast cells synchronized and arrested in S-phase of the cell cycle.

DOI: 10.7554/eLife.02678.007

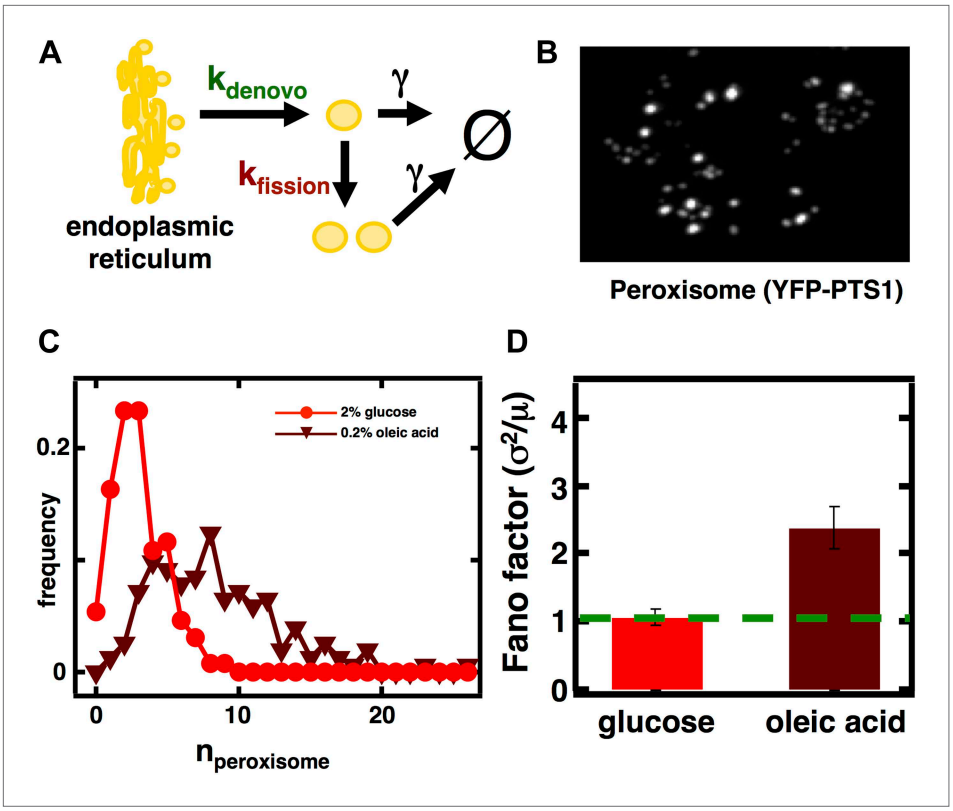

Figure 3. Inferring the dominant biophysical pathways in peroxisome biogenesis. (**A**) Schematic depicting the biophysical processes that govern peroxisome abundances. (**B**) Spinning disc confocal microscopy images of the peroxisome as visualized by the fusion protein YFP-PTS1-mRFP. (**C**) Histograms depicting experimentally measured single cell peroxisome abundance distributions for haploid cells grown in 2% glucose (red circles) and haploid cells grown in 0.2% oleic acid (dark red triangles). N = 129 cells were analyzed in glucose medium and N = 153 cells were analyzed in oleic acid medium. (**D**) Bar graph depicting measured peroxisome abundance distribution Fano factors in glucose-rich and 0.2% oleic acid-rich media. The green dashed line indicates a Fano factor $\sigma^2/\langle n \rangle = 1$, marking the boundary between de novo synthesis and fission dominated organelle production. ***Figure 3—figure supplement 1*** depicts a peroxisome biogenesis model, referred to as Model 2, alternative to the model depicted in panel (**A**). ***Figure 3—figure supplement 2*** depicts data similar to panels (**B**–**D**) but with Pex3-mRFP as the peroxisome marker. ***Figure 3—figure supplement 3*** displays simulation results from Model 2 showing how increased pre-peroxisomal vesicle production affects the mean and Fano factor of the mature peroxisome abundance distribution. ***Figure 3—figure supplement 4*** depicts the Fano factors of the Golgi apparatus and vacuole abundance distributions from cells grown in oleic acid-rich medium. Error bars are ±1 standard error of the mean, estimated by bootstrapping.

DOI: 10.7554/eLife.02678.008

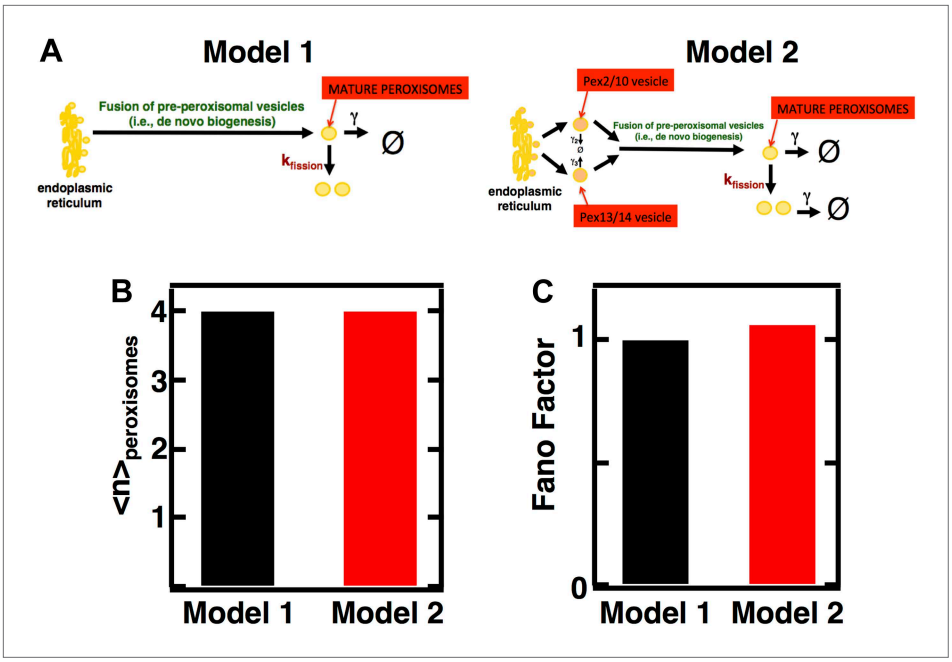

Figure 3—figure supplement 1. Incorporating pre-peroxisomal vesicle fusion into the model of de novo peroxisome biogenesis.

DOI: 10.7554/eLife.02678.009

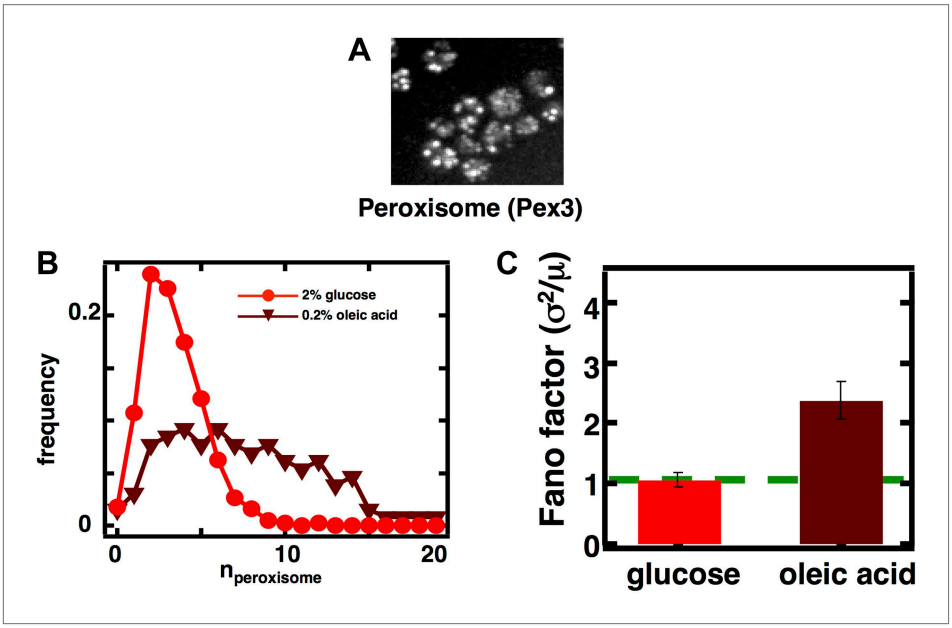

Figure 3—figure supplement 2. Measuring mature peroxisome abundance statistics using Pex3-mRFP as the peroxisomal marker.

DOI: 10.7554/eLife.02678.010

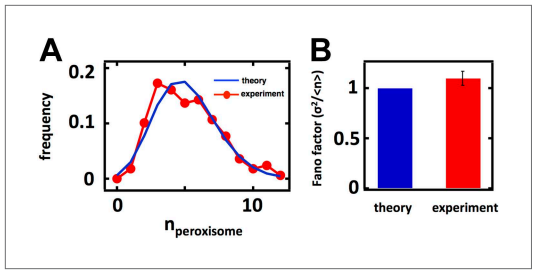

Figure 3—figure supplement 3. Predicting stochastic fluctuations in peroxisome abundance distributions in budding yeast cells synchronized and arrested in S-phase of the cell cycle.

DOI: 10.7554/eLife.02678.011

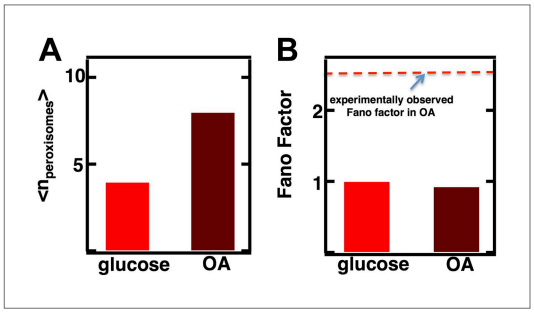

Figure 3—figure supplement 4. Effect of increasing pre-peroxisomal vesicle production in Model 2 on mean and mature peroxisome abundance distribution Fano factors.

DOI: 10.7554/eLife.02678.012

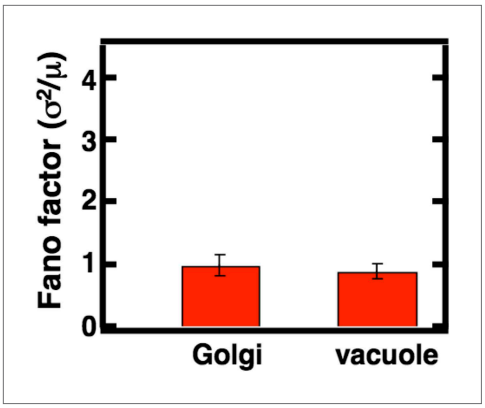

Figure 3—figure supplement 5. Golgi and vacuole abundance distribution Fano factors obtained from cells cultured in oleic acid rich medium.

DOI: 10.7554/eLife.02678.013

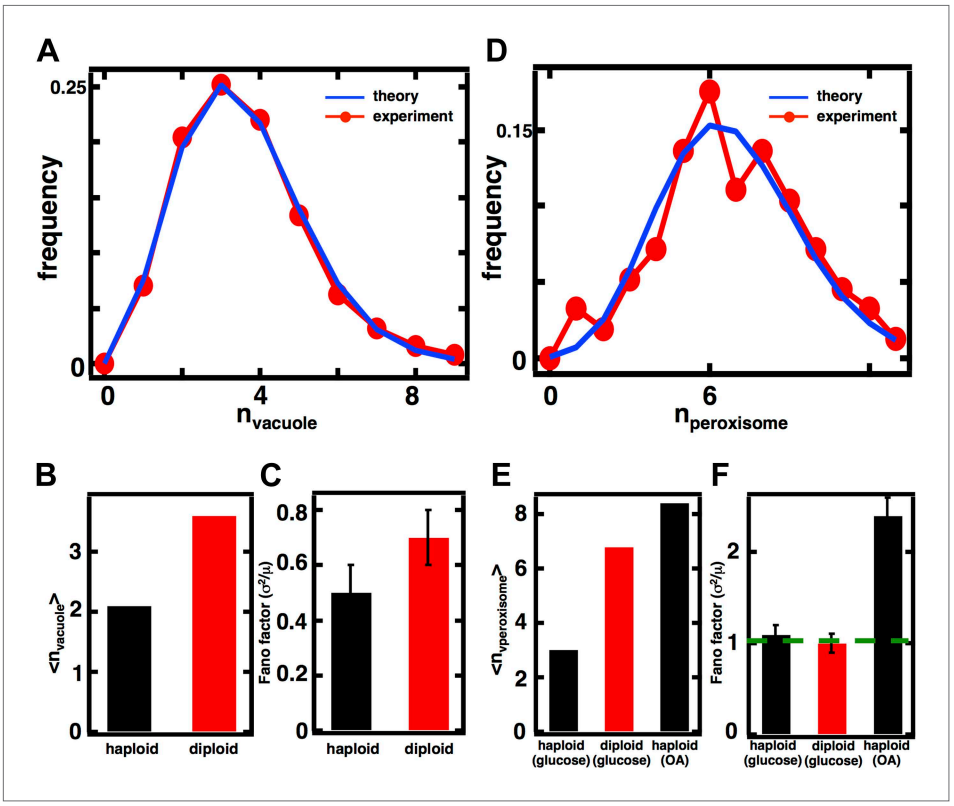

Figure 4. Predicting organelle abundance fluctuations in diploid cells. (**A**) Histograms depicting the theoretically predicted vacuole abundance distribution (blue trace) and experimentally measured single diploid cell vacuole abundance distribution (red trace). N = 127 cells were analyzed. (**B** and **C**) Bar charts comparing experimentally measured vacuole abundance means (**B**) and Fano factors (**C**) in haploid and diploid cells cultured in glucose-rich medium. (**D**) Histograms depicting the theoretically predicted peroxisome distributions (blue trace) and experimentally measured single diploid cell peroxisome abundance distributions (red trace). N = 154 cells were analyzed. (**E** and **F**) Bar charts comparing experimentally measured peroxisome means (**E**) and Fano factors (**F**) in haploid and diploid cells cultured in glucose-rich or oleic acid (OA) medium. Green line in panel (**F**) indicate Fano factor of 1. Error bars are ±1 standard error of the mean, estimated by bootstrapping. ***Figure 4—figure supplement 1*** displays the Golgi apparatus abundance distribution and its Fano factor from diploid cells grown in glucose-rich medium. ***Figure 4—figure supplement 2*** depicts data similar to panels (**D**–**F**) but with Pex3-mRFP as the peroxisome marker.

DOI: 10.7554/eLife.02678.014

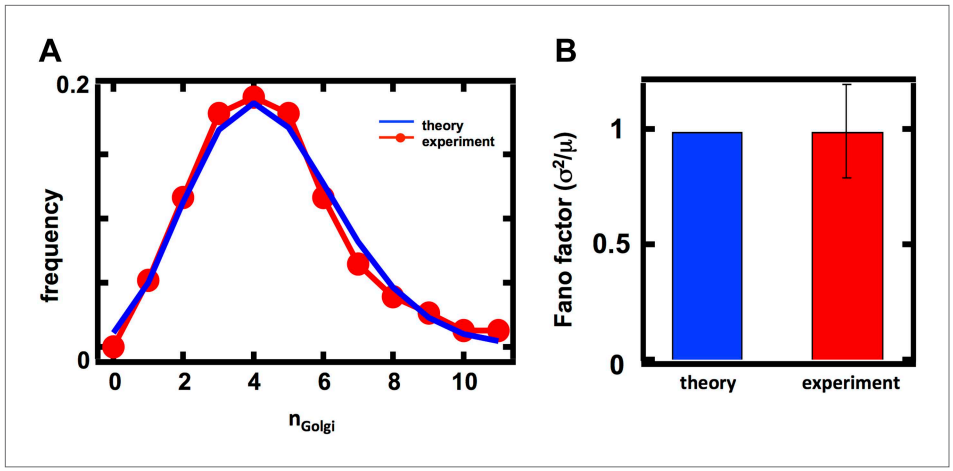

Figure 4—figure supplement 1. Golgi apparatus abundance fluctuations in diploid cells.
DOI: 10.7554/eLife.02678.015

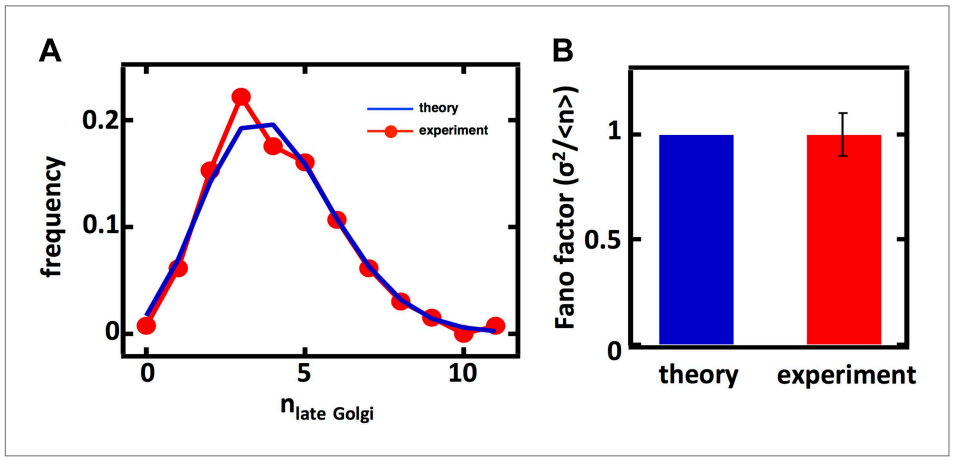

Figure 4—figure supplement 2. Late Golgi apparatus abundance fluctuations in diploid cells.
DOI: 10.7554/eLife.02678.016

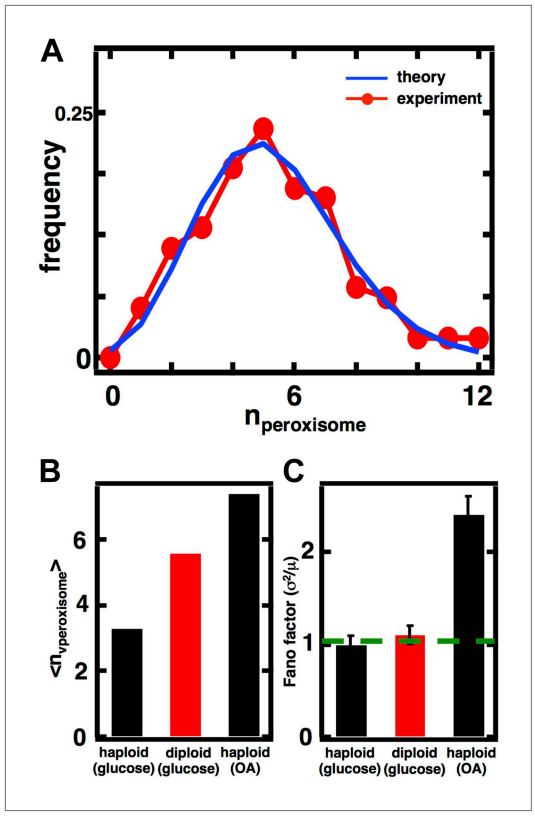

Figure 4—figure supplement 3. Peroxisome abundance fluctuations in diploid cells measured by Pex3-mRFP.

DOI: 10.7554/eLife.02678.017

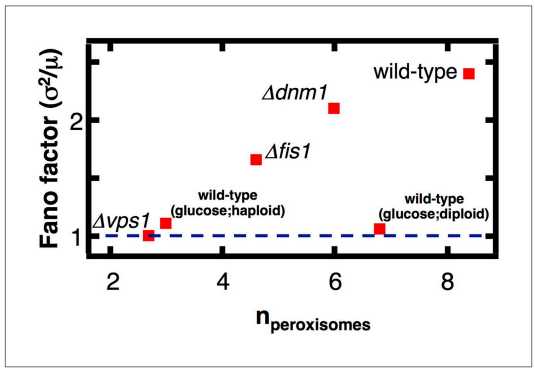

Figure 5. The effect of fission factor deletions on peroxisome abundance statistics. Budding yeast cells containing peroxisomes labeled by YFP-PTS1 and lacking one of the peroxisome fission factors *VPS1*, *DNM1* or its accessory factor *FIS1* were cultured in medium containing 0.2% oleic acid for 20 hr. Single cell peroxisome abundance distributions were measured for each of these strains. The Fano factors are plotted as a function of mean peroxisome abundance extracted from the single cell peroxisome distributions. ***Figure 5—figure supplement 1*** shows data similar to ***Figure 5*** but with Pex3-mRFP as the peroxisome marker.

DOI: 10.7554/eLife.02678.018

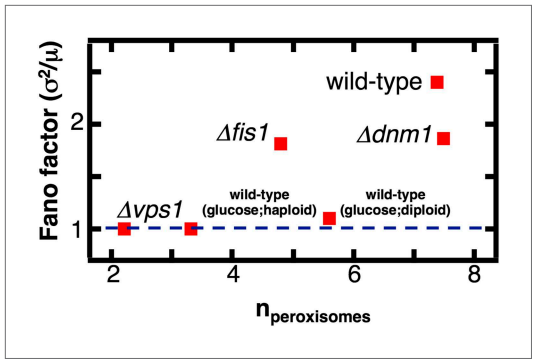

Figure 5—figure supplement 1. Peroxisome abundance fluctuations in cells containing deletions of the fission factors Dnm1, Fis1 and Vps1 measured labeling of peroxisomes by Pex3-mRFP.

DOI: 10.7554/eLife.02678.019